MATERIALS SCIENCE

Gas-liquid two-phase flow-based triboelectric nanogenerator with ultrahigh output power

Yang Dong[1,2,3]†, Shiwei Xu[1,4]†, Chi Zhang[2]†, Liqiang Zhang[1,4], Daoai Wang[1,4]*, Yuanyuan Xie[2], Ning Luo[1], Yange Feng[1,4], Nannan Wang[1], Min Feng[1], Xiaolong Zhang[3], Feng Zhou[1], Zhong Lin Wang[2,5]*

Solid-liquid triboelectric nanogenerators (SL-TENGs) have shown promising prospects in energy harvesting and application from water resources. However, the low contact separation speed, small contact area, and long contacting time during solid-liquid electrification severely limit their output properties and further applications. Here, by leveraging the rheological properties of gas-liquid two-phase flow and the Venturi-like design, we circumvent these limitations and develop a previously unknown gas-liquid two-phase flow-based TENG (GL-TENG) that can achieve ultrahigh voltage and volumetric charge density of 3789 volts and 859 millicoulombs per cubic meter, respectively. With a high-power output of 143.6 kilowatts per cubic meter, a 24-watt commercial lamp can be directly lighted by a continuous-flow GL-TENG device. The high performance displayed SL-TENGs in this work provides a promising strategy for the practical application of solid-liquid TENGs in energy harvesting and sensing applications.

INTRODUCTION

Considering that the problem of energy shortage caused by the continuous and rapid growth of the world economy is becoming increasingly prominent, renewable and clean energy solutions should be developed to alleviate possible energy crises. A large amount of renewable and clean energy is stored in natural water in the form of raindrops (*1*–*4*), rivers and ocean waves (*5*–*7*), and others (*8*–*12*). However, because of the low frequency, wide distribution areas, and irregularity of these energy sources, energy collection and utilization by traditional electromagnetic induction–based power generation equipment become difficult. The rapid development of advanced nanotechnology and nanomaterials has allowed the collection of these renewable and clean energies from water, especially the blue ocean energy (*13*). On the basis of the solid-liquid contact electrification (CE), a water-based triboelectric nanogenerator (TENG) first reported by Lin *et al.* (*14*) in 2013 opened a new chapter in the research of harvesting these energy sources from water. The TENGs combine CE and electrostatic induction effect with many advantages such as low cost, high output, environmental friendliness, and diverse material choices (*15*–*17*), attracting the attention of many researchers worldwide (*18*–*20*). Since then, an increasing number of new materials and structures have been used in solid-liquid TENGs (SL-TENGs) for energy collection from different forms of water (*21*–*26*). Xu *et al.* (*27*) developed a droplet-based electricity generator with a transistor-like architecture that can light 100 light-emitting diodes (LEDs) with a droplet of water. Wu *et al.* (*28*) fabricated a water tube–based TENG to harvest energy from waves and achieve a volumetric output charge density of 9 mC/m^3. SL-TENGs, as water energy harvesters, can provide a new solution for alleviating the problem of energy shortage. However, improving the output properties for practical applications remains challenging.

As a micro-nano energy harvester, the TENG has the advantage of high output voltage. The sustainable output voltage of the solid-solid TENG (SS-TENG) can exceed 20 kV (*29*), demonstrating an unprecedented output capability. Relevant research on SL-TENGs shows that the maximum output voltage is approximately 904 V (*30*). The lower output voltage of SL-TENGs further leads to a much lower charge density than SS-TENGs (*28*, *31*). SL-TENGs can be effectively used to harvest blue ocean energy, and their commercialization process can be promoted by increasing their output voltage and charge density. However, achieving high output voltage and charge density of SL-TENGs has always been a challenge. Because of the hydrophobic/superhydrophobicity of the surface of the contacting solid material, the liquid hardly spreads entirely on the surface. This results in a smaller solid-liquid CE area that further leads to a small surface charge density and low output. In addition, the relative separation speed of solid-liquid at the CE interface affects the output of the SL-TENGs. When other conditions are the same, the contact separation speed is proportional to its output. The relatively low separation speed of the solid-liquid interface in the traditional SL-TENGs severely limits their output. Therefore, the high output of SL-TENGs can be achieved by increasing the solid-liquid contact area and separation speed. Considering the particularity of the solid-liquid CE interface (e.g., liquid deformation and bouncing), the SL-TENGs hardly obtain a continuous and stable high output. Another shortcoming of SL- TENG is that its output depends heavily on the frequency of solid-liquid contact separation, resulting in pulsed rather than continuous output. Therefore, besides achieving high output voltage and charge density of SL-TENGs, sustainably high output should also be achieved.

Here, we developed a new gas-liquid two-phase flow-based TENG (GL-TENG) combining CE and breakdown effect, achieving a high current output of 867 μA and a high voltage output of 3789 V, which is approximately 430 and 1890 times higher than those obtained with the controlled device, respectively. The output of GL-TENG with 1.0 ml of liquid can directly power 1500 LEDs. By leveraging the

[1]State Key Laboratory of Solid Lubrication, Lanzhou Institute of Chemical Physics, Chinese Academy of Sciences, Lanzhou 730000, China. [2]CAS Center for Excellence in Nanoscience, Beijing Key Laboratory of Micro-Nano Energy and Sensor, Beijing Institute of Nanoenergy and Nanosystems, Chinese Academy of Sciences, Beijing 101400, China. [3]Hubei Key Laboratory of Hydroelectric Machinery Design & Maintenance, China Three Gorges University, Yichang 443002, China. [4]Qingdao Center of Resource Chemistry and New Materials, Qingdao 266100, China. [5]School of Materials Science and Engineering, Georgia Institute of Technology, Atlanta, GA 30332-0245, USA.
*Corresponding author. Email: wangda@licp.cas.cn (D.W.); zlwang@gatech.edu (Z.L.W.)
†These authors contributed equally to this work.

rheological properties of gas-liquid two-phase flow and the Venturi-like design, continuous and stable high-performance output can be achieved through continuous gas-liquid two-phase flow discharge. With this high output power, the output of connecting four GL-TENG devices in series can continuously drive a 24-W commercial lamp. This work not only refreshed the record of voltage output and volume charge density of SL-TENGs but also proposed a new model of gas-liquid two-phase flow-based electricity generator that can provide a strategy for efficiently collecting renewable and clean energy from water.

RESULTS

The high output performance of the GL-TENG

Figure 1A shows a schematic diagram of the GL-TENG, including the gas-liquid two-phase flow generating part, the water mist frictional electrification part, and the discharging and electric energy collecting part, corresponding to an airflow pipe, a vertical capillary tube in a water tank, a horizontal polytetrafluoroethylene (PTFE) tube, and a porous mesh conductive Ti electrode, respectively. In the gas-liquid two-phase flow generating part, a negative pressure is formed at the top of the vertical capillary when the external high-speed airflow is connected to the entrance of the horizontal PTFE tube, which has an inner diameter of 8.0 mm and an outer diameter of 10.0 mm. Under the action of pressure difference, the liquid at the bottom will be sucked out. At the same time, the sucked liquid is dispersed and atomized under the action of the strong shear force of the high-speed airflow, forming a high-speed moving gas-liquid two-phase flow. Considering the high-speed airflow shearing force and wall collision effect, the gas-liquid two-phase flow will undergo CE with the horizontal PTFE tube in the water mist frictional electrification part. The form of water and the contact state (including the contact area and relative separation speed) of the solid-liquid interface will change markedly during this process. PTFE has an excellent ability to capture charges, and the liquid is positively charged after friction (*32*, *33*). Last, the negative charges on the inner wall of the tube are transferred to the electrode using discharge in the electric energy collection part.

The dynamic balance of charge accumulation and discharge on the PTFE surface is achieved by CE and breakdown effect. A conductive path is established between the dielectric layer and the electrode when the charge accumulates enough to breakdown the interstitial dielectric (*34*). Different from the traditional air breakdown effect (*35*–*37*), the interstitial medium here refers to the gas-liquid two-phase flow. Under the same conditions, the breakdown voltage of gas-liquid two-phase flow is lower than pure air. According to Gauss's theorem, the electric field strength near the electrode can easily exceed the limit of gas-liquid two-phase flow, causing ionization of molecules (*38*–*39*). The detached electrons will be accelerated by the electric field and collide with more molecules, eventually flowing from the PTFE to the electrode. Because of the sizeable solid-liquid CE area and the fast contact separation speed, the charge accumulation on the PTFE surface is very rapid, and it only takes a dozen gas-liquid two-phase flow cycles to saturate the PTFE charge (fig. S1).

The electrode in this part is a regular circular porous mesh conductive Ti with a diameter of 2 cm and a thickness of 1 mm printed by a three-dimensional (3D) printer, and this porous mesh structure can substantially increase the contact area of solid-liquid discharge

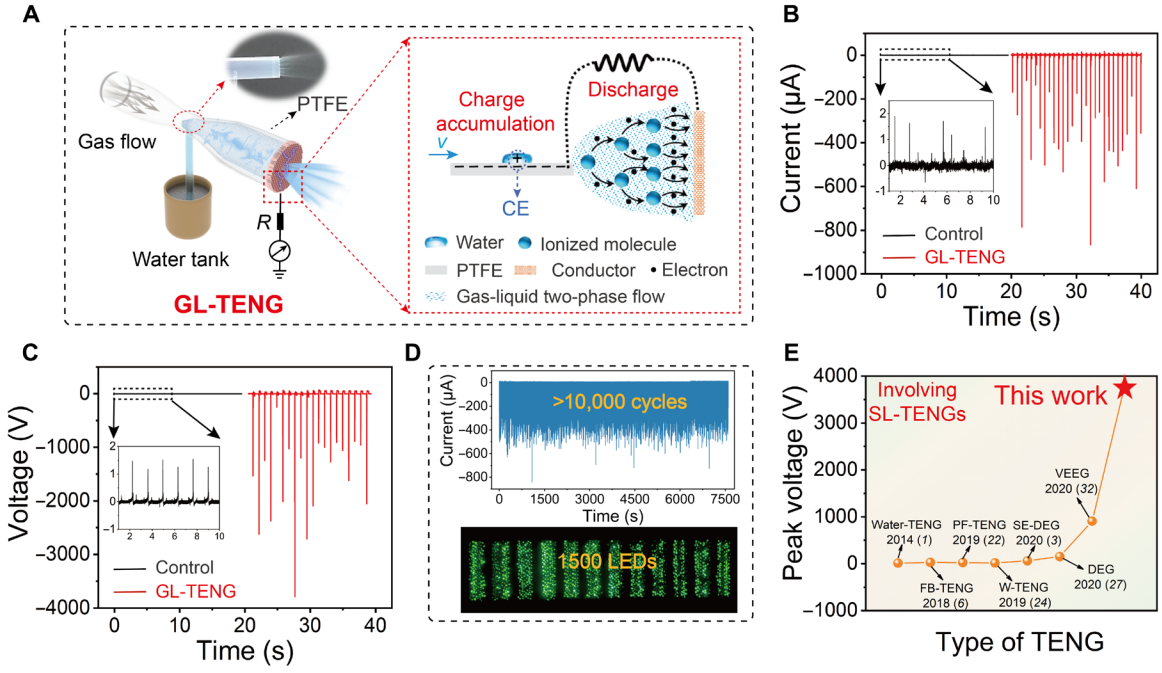

Fig. 1. Structural design and performance of the GL-TENG. (**A**) Schematic diagram of GL-TENG and a detailed discharge effect mechanism. The inserts show the corresponding partial physical diagrams. PTFE, polytetrafluoroethylene. (**B**) Comparison of current output between GL-TENG (in red) and the control device (in black). (**C**) Peak voltage output of GL-TENG (in red) is more than three orders of magnitude higher than that from the control device (in black). (**D**) Stability test of GL-TENG with a continuous jet-on time of 0.2 s and a jet-off time of 0.5 s for more than 10,000 cycles, and 1500 LEDs can be powered when 1.0 ml of liquid is used by the GL-TENG. (**E**) Comparison of the peak voltage value obtained in this work with other reports. SL-TENG, solid-liquid TENG. PF-TENG, Pulsatile Flow-triboelectric nanogenerator; SE-DEG, single electrode droplet-based electricity generator; FB-TENG, floating buoy-based triboelectric nanogenerator; W-TENG, water-solid triboelectric nanogenerator; VEEG, volume-effect electricity generator; DEG, droplet-based electricity generator.

and capture electric energy with high probability. Notably, each of these three parts is essential for the operation of the GL-TENG device. The whole structural design of GL-TENG can make full use of the rheological properties of the fluid to increase the solid-liquid CE area and significantly increase the relative speed of solid-liquid contact separation. Both of these phenomena are vital factors that promote solid-liquid CE.

To facilitate the collection of blue ocean energy, we used different concentrations of NaCl solution to simulate seawater and successfully collected clean energy from the liquid. The high-speed airflow pressure of the external compressed air system connected to the GL-TENG device was 0.8 MPa, and the maximum airflow velocity ejected from the nozzle can reach 35.0 m/s. During the test, the jet velocity was maintained at the maximum of 35.0 m/s, and a typical frequency with a continuous jet-on time of 0.2 s and a jet-off time of 0.5 s to maintain regular discharge. Under this condition, the volume of the atomized liquid in a single cycle was approximately 1.0 ml. Exciting experimental results were obtained when a NaCl solution (0.5 mol/liter) was used for the test. Focusing on a single cycle of the GL-TENG device indicates that the maximum peak short-circuit output current and maximum peak open-circuit output voltage were approximately 867 μA (Fig. 1B) and 3789 V (Fig. 1C), respectively, which are 430 and 1890 times higher than those obtained with the "controlled" device (fig. S2). As shown in Fig. 1D, the GL-TENG device can operate continuously for more than 10,000 cycles with good stability without decay. Using the GL-TENG device, 1500 LEDs can be lighted up easily. In comparison with the previously reported voltage value of SL-TENGs, the outputs of GL-TENG are also much higher (Fig. 1E and table S1).

Working principle of the GL-TENG

On the basis of the peak shape of current (fig. S3) and voltage (fig. S4) output in a single cycle, GL-TENG shows breakdown behavior, but the specific breakdown peaks shape is random. To further understand the working mechanism of GL-TENG, we conducted an in-depth analysis of the first relatively regular current and voltage shape. Careful inspections (Fig. 2, A and B) show two discharge processes, including discharge of negative ($t_0 - t_1$) and discharge of positive ($t_1 - t_2$) due to the breakdown effect and positively charged gas-liquid two-phase flow discharge, respectively. The instantaneous maximum current in discharge II was approximately 124 times that of the discharge III, but the duration of the discharge was $^1/_{15}$ of discharge III. As plotted in Fig. 2C, at the initial time (t_0) of the discharge II, a sharp increase was observed in the measured charges and reached the maximum value, with Q_{max}(II) of −859.0 nC. In the following process of discharge III, the polarity of the charges changed and reached the maximum value, with Q_{max}(III) of about 800.0 nC (fig. S5A). Analysis of the transferred charges in nearly 300 cycles show that the average transferred charge value of processes II and III were approximately −361.6 and 341.4 nC (fig. S5B), respectively. Therefore, the total amount of positive and negative charges is basically conserved, and the slight difference is caused by the free dissipation of charges and part of the charges not being captured by the porous mesh electrode. These results show that the GL-TENG device can output a large amount of charge in a very short time of 0.02 s to achieve a volumetric output charge density of up to 859 mC/m^3 and power density output reaches 143.6 kW/m^3, respectively, which are much higher than other previous reports (fig. S6). Moreover, not

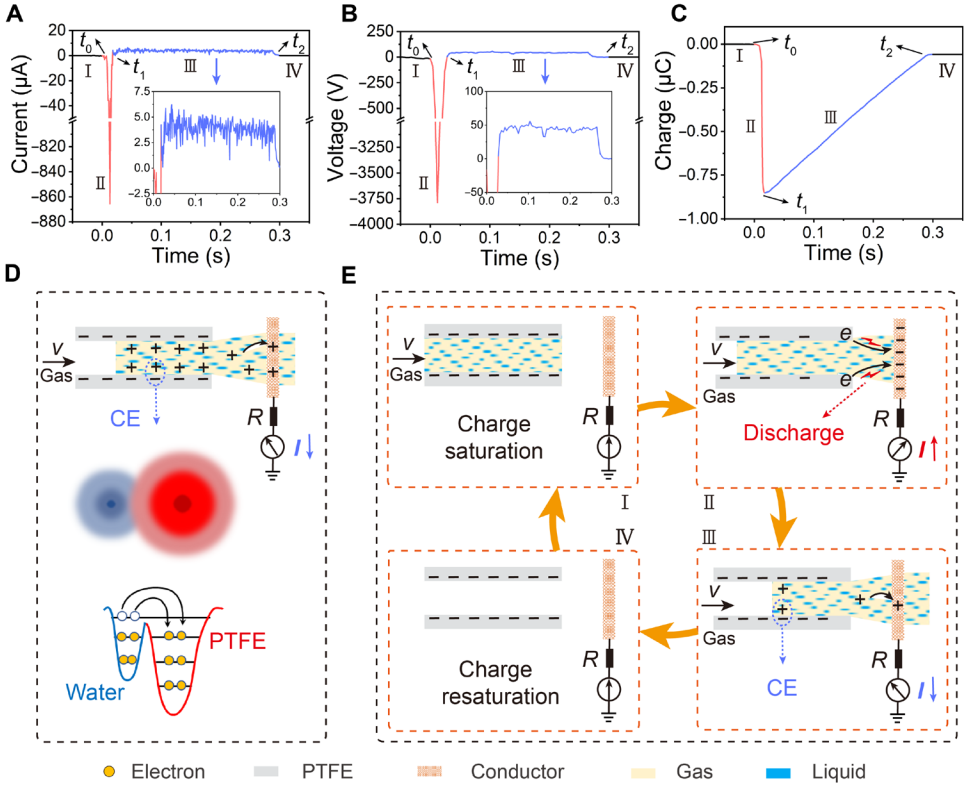

Fig. 2. Working principle of the GL-TENG. (**A**) Generated current, (**B**) voltage, and (**C**) transferred charge from the GL-TENG during one gas-liquid two-phase flowing process cycle. (**D**) Schematic diagram of the working principle of the initial charge accumulation process and (**E**) the steady operation process. CE, contact electrification.

every discharge is high and stable, as shown in fig. S7. In addition, the output voltage remains constant when the porous Ti electrode is replaced by a Cu or Fe electrode, indicating that electricity generation is not sensitive to the specific electrode materials, as shown in fig. S8.

CE occurs when water and PTFE are in close contact, and electrons flow from water to PTFE. Negative charges will quickly accumulate on the inner surface of PTFE tube, the positively charged gas-liquid two-phase flow will discharge when it contacts the conductive electrode, and electrons flow from the ground to the water to generate a positive dc voltage (Fig. 2D). More detailed mechanisms can be found in fig. S9. A discharge will occur when the negative charges accumulate enough on the PTFE surface, resulting in an ac voltage output.

During the steady operation process of GL-TENG, initially, as shown in Fig. 2E (state I), CE will not occur when liquid flows through PTFE that is saturated with negative charges. At this time, the electric field strength of the accumulated charges on the PTFE surface is insufficient to cause the discharge effect, the external circuit will not generate current and voltage output. With the generation of the gas-liquid two-phase flow at the outlet, the gas-liquid two-phase flow will replace the air and fill the gap between the dielectric layer and the electrode in a very short time (state II). Because of the ability of water molecules to form negative ions, the gas-liquid two-phase flow is more prone to the breakdown discharge than the air (*40*). Considering the electric field strength formed by the accumulated charge of PTFE is sufficient to breakdown the gas-liquid two-phase flow and generate a huge discharge. The current and voltage then exhibit a large acceleration with a pronounced peak of up to −867 μA and −3789 V at a time (t_0) of 0 s, transitioning into a "jet-on" state. With the discharge occurring, the charge on the PTFE surface is no longer saturated. At this time, the contact of water with PTFE will cause CE and electrons flow from the water to the PTFE, forming a positively charged gas-liquid two-phase flow (state III). The solid-liquid CE causes the charge on the PTFE surface to reaccumulate until saturation is reached again (state IV). If the PTFE tube is regarded as a capacitor during GL-TENG operation, then the dynamic balance of charge accumulation and discharge is achieved through solid-liquid CE and discharge. Its detailed mechanism also can be seen in fig. S10.

Performance of the GL-TENG under different conditions

To further investigate the vast improvement in the output performance of the GL-TENG over the control device, we first analyzed the generation of gas-liquid two-phase flow and the dynamic process of its movement in the PTFE tube. When the GL-TENG is in a jet-on state, negative pressure forms in the space near the top of the vertical capillary tube because of reducing the cross-sectional area of the gas flow. The negative pressure has an adsorption effect on the water in the bottom tank, and a small amount of water is sucked out under the adsorption force. The sucked water undergoes a series of complex physical processes such as deformation and breaking under the strong shear force of the high-speed airflow and lastly forms a high-speed moving gas-liquid two-phase flow. It further undergoes a complex deformation process under the combined action of the airflow shear effect and the tube wall collision effect (movies S1 and S2). On the basis of the generation of the gas-liquid two-phase flow and its movement in the tube (Fig. 3, A and B), the liquid sucked out by the negative pressure was dispersed into numerous tiny droplets and flowed rapidly on the PTFE wall. Their motions on the tube wall are not always continuous, but each liquid presents a cell-like flow, as shown in fig. S11 and movie S3. During the movement of water mist on the wall of the hydrophobic PTFE tube, it may break up again or fuse. The solid-liquid contact area and relative separation speed between water and PTFE are much larger than the control device through this specific deformation process.

In addition, we simulated the pressure distribution of the gas-liquid two-phase flow in the tube at different gas flow velocities, as shown in Fig. 3C. This figure shows that the greater the speed, the greater the negative pressure formed at the water outlet of the vertical pipe. High velocity directly results in a higher amount of water gas-liquid two-phase flowed and higher velocity within the tube. Under the same conditions, we also calculated by density functional theory (DFT) simulation that the amount of charge transferred between the water and PTFE will increase after adding a small amount of NaCl (Fig. 3D), consistent with the previous experimental results. When a small amount of NaCl is added, the ion concentration in the solution increases slightly, and the charge transfer ability of the solution increases. However, when the ion concentration in the solution increases, the charge dissipation becomes stronger due to the rapid rise of the liquid conductivity, which seems to be unfavorable for the generation of triboelectric charges. However, at this time, due to the introduction of ions, the charge on the inner wall of PTFE is easier to discharge to the electrode through the gas-liquid two-phase flow.

Before the experiment, all PTFE tubes were ultrasonically cleaned with ethanol and deionized (DI) water for 10 min. After drying, an ion fan was used to process the entire system to eliminate the interference of preaccumulated charges. Different external airflow velocities and different types of friction materials are used to demonstrate the performance of the GL-TENG further. The pressure of the jet is maintained at 0.8 MPa, and the jet velocity can be changed from 0 to 35 m/s by adjusting the opening of the air valve. We measured the output performance of GL-TENG by using a NaCl solution and PTFE as friction material based on different external airflow velocities of 10, 18, 25, 30, and 35 m/s (Fig. 3, E to G). The airflow velocity greatly influenced the output of GL-TENG and increased with the increase of airflow velocity. This phenomenon was observed, because the change in the airflow velocity connected to the GL-TENG from the outside directly caused the formed gas-liquid two-phase flow velocity and the liquid atomization volume to change considerably. The increase in flow velocity further increased the solid-liquid contact separation speed and electrification area, resulting in a larger output.

The frequency of the jet has almost no effect on the peak voltage and current (fig. S12, A and B) output of the GL-TENG. However, the longer the state of jet-on in a single cycle, the higher the amount of charge transferred, as shown in fig. S12C. Part of the details of GL-TENG output can also be seen in fig. S13. In addition, the output of GL-TENG is not sensitive to the material of the vertical capillary tube (fig. S14) but has a significant dependence on the material of the horizontal tube. We measured the GL-TENG output performance based on DI water and various solid materials (Fig. 3, H to J), including PTFE, polyvinyl chloride (PVC), polylactic acid (PLA), nylon, Fe, and Cu. According to the signals of different friction solid materials, the output relies on the polarity of the triboelectric material (*41*, *42*). Considering that PTFE has a very strong ability to obtain electrons and store charges compared with other materials, the output of choosing PTFE is the largest and much higher than the others. In addition, we tested the output performance of GL-TENG

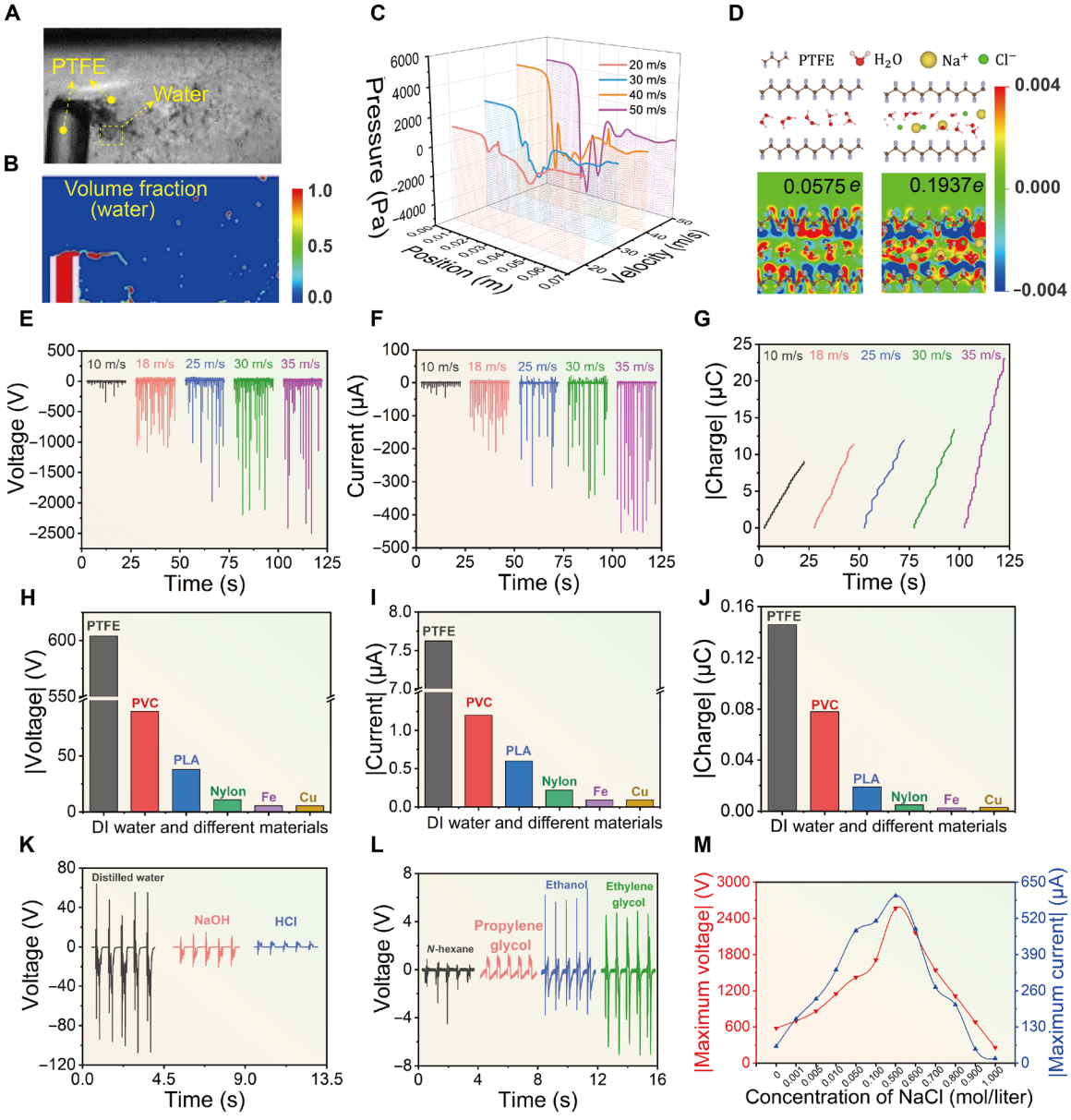

Fig. 3. Output performances of the GL-TENG. (**A**) Dynamic photo of gas-liquid two-phase flow generation and movement within the tube. (**B**) Simulation of the liquid volume fraction based on Ansys Fluent. (**C**) Positional-dependent pressure simulation of gas-liquid two-phase flow in the GL-TENG tube at different velocities. (**D**) Simulation of solid-liquid charge transfer based on density functional theory (DFT). (**E** to **G**) The output performances of GL-TENG based on different external airflow velocities. (**H** to **J**) The output performances of GL-TENG based on different solid friction materials. (**K** to **M**) The output performances of GL-TENG based on different liquid friction materials. DI, deionized; PVC, polyvinyl chloride; PLA, polylactic acid.

based on PTFE and different liquids, including acid and base such as NaOH (0.90 mol/liter) and HCl (0.35 mol/liter) (Fig. 3K); organics such as *n*-hexane, propylene glycol, ethanol, and ethylene glycol (Fig. 3L); and salt solution with different concentrations of NaCl (Fig. 3M). The results show that distilled water has a higher output than acidic and alkaline solutions, while nonpolar organic solvent solutions have a lower output than other polar aqueous solutions. The output of GL-TENG first increased and then decreased with the increase of the concentration of NaCl solution, indicating that the addition of an appropriate amount of neutral ions to the aqueous solution will remarkably promote the output.

To better understand the results of Fig. 3 (K to M), careful analysis is required from the two aspects of CE and discharge. In terms of CE, the ions in aqueous solution have significantly different effects on CE (*43*–*44*). Generally speaking, the solution in the low concentration range will promote the charge transfer at the interface, while the solution with higher concentration will inhibit the charge transfer at the interface (*45*–*46*). When ions are present in water, charge transfer occurs at the solid-liquid interface via electron and ion transfer (*47*). A slight increase in ionic concentration salt solutions can facilitate charge transfer. In addition, a further increase in ion concentration would lead to excessive free ions in the solution and further lead to

the inhibition of CE (Fig. 3M). For the CE between organic solvents and PTFE, the difference in the ability of the two to gain and lose electrons is relatively small, further resulting in relatively small charge transfer. In terms of discharge, high concentration of NaCl leads to a decrease in the discharge voltage threshold between the electric field formed by the accumulation of charges on the PTFE and the external electrode, making the discharge more likely to occur. The voltage threshold of the formed two-phase flow also undergoes complex changes for different organics (Fig. 3L). With the increase of NaCl concentration in the solution, the voltage threshold of GL-TENG for discharge showed a complex trend of first increasing and then decreasing (Fig. 3M). It may be that triboelectric charging and electrostatic discharge have a coupling effect on the output of GL-TENG, resulting in an optimal concentration range. Therefore, different ions have dual effects on the output of GL-TENG, and the specific analysis needs to be comprehensively considered in combination with CE and discharge.

Demonstration of the high-performance of the GL-TENG

In addition to pulse mode GL-TENG, the output of continuous-flow GL-TENG can directly power electronic devices. Similar to the previous description in Fig. 1A, the continuous-flow GL-TENG mainly includes water mist frictional electrification and the discharging and electric energy collection. Notably, the continuous-flow GL-TENG is universal in practical applications and has the advantages of continuous high output. When the GL-TENG is in the "jet-off" state, there will be no gas-liquid two-phase flow and power output. Ultrahigh output can be obtained when transformed into the jet-on state. Keeping the continuous-flow GL-TENG in the state of jet-on can obtain continuous and stable voltage and current (Fig. 4, A and B). As shown in Fig. 4A, we conducted a long-term stability test on the continuous-flow GL-TENG device, and the results showed that such a high and stable output could charge different capacitors and drive low-power electronic devices after rectification (fig. S15). From the current signal within 1 s (Fig. 4B), the discharge frequency of the large current is very high, which further illustrates the superiority of the continuous-flow GL-TENG in terms of continuous and stable output. According to the above analysis, a simulation circuit model was proposed, as shown in Fig. 4 (C and D). First, a current source and an internal capacitor are proposed to demonstrate the effect of solid-liquid CE, while a diode is added to describe the "unidirectional" nature of the discharge process. Later, a voltage-controlled resistor was proposed to represent the variable path resistance in different states. When little charge accumulates on the PTFE, representing the charge accumulation stage shown in Fig. 4C, the interstitial medium (gas-liquid two-phase flow) between the PTFE dielectric layer and the electrode is not ionized, so that the resistance is considerable and behaves like an insulator. Continued CE results in enough charge accumulation on the PTFE surface that the voltage exceeds the critical ionization voltage, representing the discharge

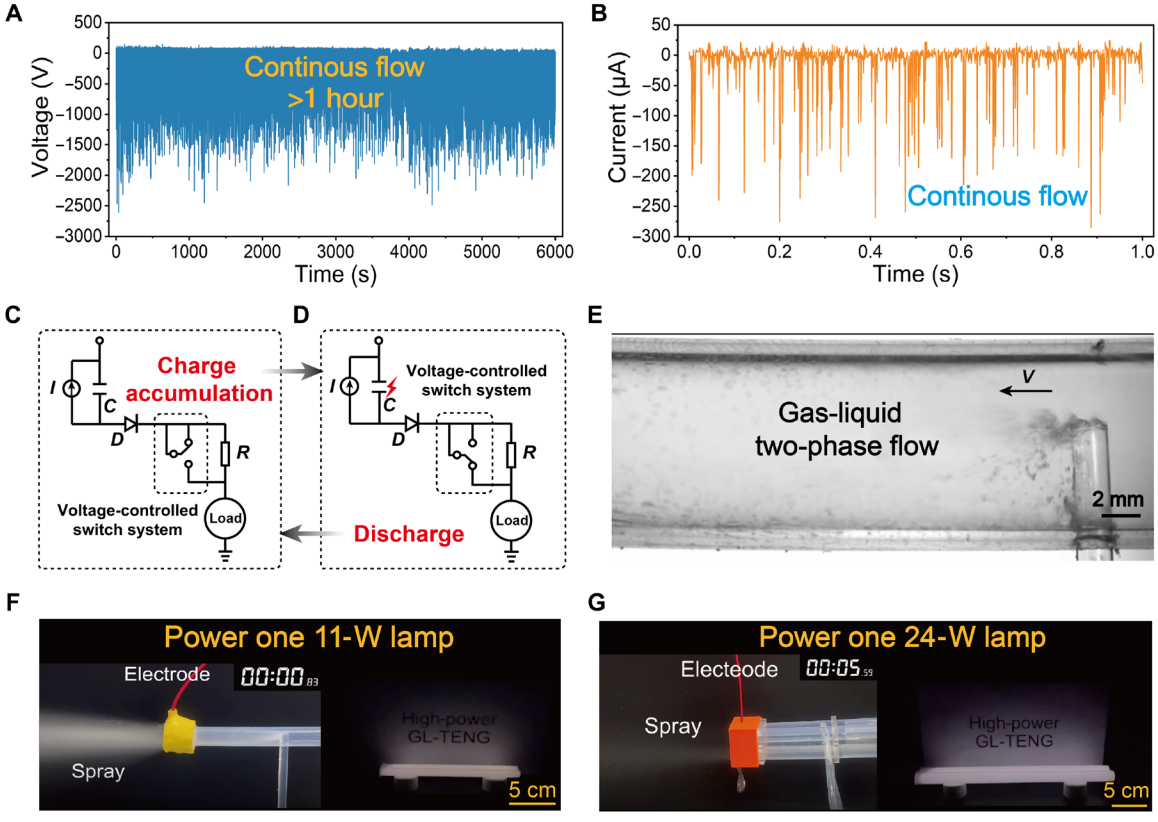

Fig. 4. Application of the GL-TENG to drive electronic devices. (**A**) Output voltage and stability test of the continuous-flow GL-TENG (load resistance of 100 megohms). (**B**) Current output when the continuous-flow GL-TENG is in the jet-on state. (**C**) Simulation circuit model of charge accumulation and (**D**) discharge of the continuous-flow GL-TENG. (**E**) High-speed camera shooting: Motion of gas-liquid two-phase flow in the pipeline. (**F**) One 11-W commercial lamp was directly powered by continuous-flow GL-TENG devices. (**G**) One 24-W commercial lamp was continuously powered by four continuous-flow GL-TENG devices connected in series.

phase shown in Fig. 4D. At the same time, the voltage between the PTFE dielectric layer and the electrode exceeded the breakdown limit, and the resistance dropped sharply to near zero, representing a short circuit in the breakdown path. Last, the charge accumulation and discharge of the continuous-flow GL-TENG are in dynamic equilibrium during operation through CE and breakdown discharge effect.

As shown in Fig. 4E, the motion process of the gas-liquid two-phase flow in the tube was captured by a high-speed camera at a typical recording speed of 30,000 frames per second (movie S1), which can help to understand the reason for the high output. Leveraging on the ultrahigh output, we succeeded continuously in powering an 11-W commercial lamp (Fig. 4F and movie S4). In addition, it can be connected in series to continuously power higher power electronic equipment without any additional auxiliary devices. As a further improvement, we successfully continuously powered a 24-W commercial lamp with the output of four continuous-flow GL-TENG devices connected in series (Fig. 4G and movie S5). The GL-TENG was first used to power a commercial lamp in the present study.

Considering that the output of the GL-TENG is an alternating current, it is difficult to directly use the long/positive/low discharge (III) generated by GL-TENG (fig. S15A). To fully use the output of GL-TENG, a rectifier bridge is added to the external circuit as shown in fig. S15B. After rectification, the current output will become a dc signal (fig. S15C). In this way, the ac output of the GL-TENG can be turned into a dc output. The results shown in fig. S15D were obtained by driving 25 LEDs with the output before and after rectification, respectively. Excitingly, the output after rectification is more sustainable than the output before rectification when driving electronic devices, which is benefited from the full utilization of the electricity power [including the short/negative/high discharge (II) and the long/positive/low discharge (III)] generated by GL-TENG after rectification (movie S6). In addition, the rectified output can also directly charge a series of capacitors, and the stored electricity can be used to drive low-power electronic devices such as watches (fig. S15E). The electricity stored in the capacitors can also be directly used to drive other microelectronic devices or systems so as to fully use the electricity generated by GL-TENG.

DISCUSSION

In the present work, combining CE and breakdown effect, we propose the GL-TENG device for boosting the power output of the SL-TENGs by significantly increasing the solid-liquid CE area and relative separation speed. An ultrahigh voltage output of −3789 V and ultrahigh volumetric output charge density of −859 mC/m^3 were achieved, which remarkably differ from previous studies. With the ultrahigh power output of GL-TENG, we directly lighted 1500 LEDs and a 24-W commercial lamp, respectively. The GL-TENG has developed a new gas-liquid two-phase flow-based model of an electricity generator and demonstrated the ability to drive various electronic devices directly. It also provides a new strategy for efficiently harvesting energy from water and opens up an avenue for future commercial use for SL-TENGs.

MATERIALS AND METHODS

Materials

Porous titanium electrode was printed using a 3D printer. DI water was obtained from a laboratory water purification system (Spring R10). NaCl (99.5%) and ethanol (99.7%) were obtained from Tianjin Dingshengxin Chemical Industry Co. Ltd. Pipes of different diameters (e.g., 1 mm by 2 mm, 6 mm by 8 mm, and 20 mm by 25 mm) and different materials (e.g., PTFE, PVC, Cu, Fe, fiberglass, polypropylene (PP), polymethyl methacrylate, and nylon) were obtained from Yangzhong Fuda Insulation Electric Co. Ltd. and native stores.

Fabrication of GL-TENG device

To fabricate the GL-TENG, the porous conductive electrode and the pipes were first ultrasonically cleaned with ethanol and DI water for 10 min. The device is mainly composed of a porous conductive electrode, horizontal tube, vertical capillary tube, and insulated water tank at the bottom, as shown in Fig. 1A. The inner and outer diameter of the vertical capillary tube is 1 mm by 2 mm, while the inner and outer diameter of the horizontal tube is gradually changed from 8 mm by 10 mm to 20 mm by 25 mm. At the inlet of GL-TENG, a high-pressure jet (0.8 MPa) with controllable frequency and speed generated by the air compression control system is connected. Considering that the bottom pressure of the vertical capillary tube is stronger than the top pressure during operation, the water is forced out under the action of the pressure difference. The gas-liquid two-phase flowed water lastly forms a gas-liquid two-phase flow under the action of the high-speed airflow. Considering the greatly enlarged solid-liquid friction contact area and solid-liquid friction separation speed, the process of gas-liquid two-phase flowing water out of atomization is accompanied by a large amount of electron transfer. At the outlet of GL-TENG, a 3D printed porous titanium with good conductivity and corrosion resistance (a diameter of 20 mm and a thickness of 0.5 mm) is used as a conductive electrode.

Characterization and measurement

The air compression control system was used to generate high-pressure airflow with controllable speed and frequency. When keeping the jet on for 0.2 s and off for 0.5 s, the average gas-liquid two-phase flow volume of a vertical capillary with an inner diameter of 1 mm and an outer diameter of 2 mm is approximately 1.0 ml per cycle. Sodium chloride and DI water were used for the preparation of NaCl solutions with different concentration gradients. Liquid gas-liquid two-phase flowing and its movement in the tube are recorded by a high-speed camera (Revealer) at a typical recording speed of 30,000 frames per second. The velocity of high-speed airflow was measured by a hot wire anemometer (AR866A). The output voltage of GL-TENG was measured using a 3 Series mixed domain oscilloscope with a high-impedance (100 megohms) probe, while the current was measured via an SR570 low-noise current preamplifier (Stanford Research Systems). Data were collected through LabVIEW Base Development System (National Instruments).

Ansys Fluent simulation

First, we use the professional fluid simulation analysis software Ansys Fluent to simplify the 2D modeling of the GL-TENG. As shown in fig. S16A, the inner diameter of the horizontal pipe is 8 mm and the length is 0.07 m. A vertical capillary with an inner diameter of 1 mm is connected at a distance of 0.02 m from the gas inlet. The distance between its exposed height and the lower end of the pipe wall is 3 mm. In the simulation, the set inlet velocities were set as 20, 30, 40, and 50 m/s, respectively, and the no-slip boundary condition is set on the pipe wall. When the high-speed airflow passes through the upper end of the vertical capillary tube, a negative pressure will be

formed to adsorb the water in the water tank, and lastly, a gas-liquid two-phase flow will flow out from the tube outlet. Taking the air inlet as the coordinate zero point and the horizontal rightward as the positive direction of the *x* axis, the curve of the pressure change with the location on the central section of the horizontal pipe is obtained. The results show that the pressure decreases sharply at the intersection of the two pipes and eventually stabilizes (fig. S16B). In addition, the dynamic process of gas-liquid two-phase flow in GL-TENG was simulated as shown in movie S2.

DFT simulation

In our model, the model of PTFE and water without or with a small amount of NaCl was established, which was shown in Fig. 3D. The periodic boundary conditions are applied in the *x* and *y* directions, and a vacuum region was about 20 Å in the *z* direction. All computations are performed within the framework of DFT as implemented in the Vienna Ab initio Simulation Package code by using the projector augmented wave method with the Perdew-Burke-Ernzerhof exchange-correlation functional (*48*–*50*), and the plane wave energy cutoff is set to 500 eV. The influence of van der Waals interactions is considered by using DFT-D3, which is developed by Grimme *et al.* (*51*). For all relaxation processes, special Γ-centered *k* points sampled on a 3× 3 × 1 mesh are used. The whole structures are relaxed by using a conjugate gradient algorithm until the force on each atom is less than 0.01 eV/Å. To explore the amount of charge transferred between the PTFE and water without or with small amount of NaCl, 2D projections of the charge density differences (in units of e·Å^{-3}) were calculated by $\Delta\rho = \rho_{PTFE + H_2O(NaCl)} - \rho_{PTFE} - \rho_{H_2O(NaCl)}$. Here, $\rho_{PTFE + H_2O(NaCl)}$ is the total charge density of the whole system, and ρ_{PTFE} and $\rho_{H_2O(NaCl)}$are the charge densities of PTFE and water without or with NaCl, respectively. The DTF simulation shows that charge is transferred between the PTFE and water. The Bader charges (*52*–*55*) further give that the amount of charge transfer between the water and PTFE will increase after adding a small amount of NaCl (Fig. 3D), consistent with the previous experimental results.

SUPPLEMENTARY MATERIALS

Supplementary material for this article is available at https://science.org/doi/10.1126/sciadv.add0464

View/request a protocol for this paper from *Bio-protocol*.

REFERENCES AND NOTES

1. Z.-H. Lin, G. Cheng, S. Lee, K. C. Pradel, Z. L. Wang, Harvesting water drop energy by a sequential contact-electrification and electrostatic-induction process. *Adv. Mater.* **26**, 4690–4696 (2014).
2. Y. Liu, N. Sun, J. Liu, Z. Wen, X. Sun, S.-T. Lee, B. Sun, Integrating a silicon solar cell with a triboelectric nanogenerator via a mutual electrode for harvesting energy from sunlight and raindrops. *ACS Nano* **12**, 2893–2899 (2018).
3. N. Zhang, H. Gu, K. Lu, S. Ye, W. Xu, H. Zheng, Y. Song, C. Liu, J. Jiao, Z. Wang, X. Zhou, A universal single electrode droplet-based electricity generator (SE-DEG) for water kinetic energy harvesting. *Nano Energy* **82**, 105735 (2021).
4. D. Choi, D. W. Kim, D. Yoo, K. J. Cha, M. La, D. S. Kim, Spontaneous occurrence of liquid-solid contact electrification in nature: Toward a robust triboelectric nanogenerator inspired by the natural lotus leaf. *Nano Energy* **36**, 250–259 (2017).
5. Y. S. G. Zhu, P. Bai, J. Chen, Q. Jing, W. Yang, Z. L. Wang, Harvesting water wave energy by asymmetric screening of electrostatic charges on a nanostructured hydrophobic thin-film surface. *ACS Nano* **8**, 6031–6037 (2014).
6. D. Y. Kim, H. S. Kim, D. S. Kong, M. Choi, H. B. Kim, J.-H. Lee, G. Murillo, M. Lee, S. S. Kim, J. H. Jung, Floating buoy-based triboelectric nanogenerator for an effective vibrational energy harvesting from irregular and random water waves in wild sea. *Nano Energy* **45**, 247–254 (2018).
7. J. Scruggs, P. Jacob, Harvesting ocean wave energy. *Science* **323**, 1176–1178 (2009).
8. Y. Huang, H. Cheng, C. Yang, P. Zhang, Q. Liao, H. Yao, G. Shi, L. Qu, Interface-mediated hygroelectric generator with an output voltage approaching 1.5 volts. *Nat. Commun.* **9**, 41466 (2018).
9. X. Chen, D. Goodnight, Z. Gao, A. H. Cavusoglu, N. Sabharwal, M. DeLay, A. Driks, O. Sahin, Scaling up nanoscale water-driven energy conversion into evaporation-driven engines and generators. *Nat. Commun.* **6**, 7346 (2015).
10. J. Xiong, M.-F. Lin, J. Wang, S. L. Gaw, K. Parida, P. S. Lee, Wearable all-fabric-based triboelectric generator for water energy harvesting. *Adv. Energy Mater.* **7**, 1701243 (2017).
11. J. Chung, D. Heo, G. Shin, S.-H. Chung, J. Hong, S. Lee, Water behavior based electric generation via charge separation. *Nano Energy* **82**, 105687 (2021).
12. T. B. H. Schroeder, A. Guha, A. Lamoureux, G. VanRenterghem, D. Sept, M. Shtein, J. Yang, M. Mayer, An electric-eel-inspired soft power source from stacked hydrogels. *Nature* **552**, 214–218 (2017).
13. Z. L. Wang, Catch wave power in floating nets. *Nature* **542**, 159–160 (2017).
14. Z.-H. Lin, G. Cheng, L. Lin, S. Lee, Z. L. Wang, Water-solid surface contact electrification and its use for harvesting liquid-wave energy. *Angew. Chem. Int. Ed. Engl.* **52**, 12545–12549 (2013).
15. Z. L. Wang, J. Chen, L. Lin, Progress in triboelectric nanogenerators as a new energy technology and self-powered sensors. *Energy Environ. Sci.* **8**, 2250–2282 (2015).
16. J. Xiong, P. Cui, X. Chen, J. Wang, K. Parida, M. F. Lin, P. S. Lee, Skin-touch-actuated textile-based triboelectric nanogenerator with black phosphorus for durable biomechanical energy harvesting. *Nat. Commun.* **9**, 4280 (2018).
17. S. Park, H. Kim, M. Vosgueritchian, S. Cheon, H. Kim, J. H. Koo, T. R. Kim, S. Lee, G. Schwartz, H. Chang, Z. Bao, Stretchable energy-harvesting tactile electronic skin capable of differentiating multiple mechanical stimuli modes. *Adv. Mater.* **26**, 7324–7332 (2014).
18. W. Li, D. Torres, R. Díaz, Z. Wang, C. Wu, C. Wang, Z. L. Wang, N. Sepúlveda, Nanogenerator-based dual-functional and self-powered thin patch loudspeaker or microphone for flexible electronics. *Nat. Commun.* **8**, 15310 (2017).
19. Y. Zi, S. Niu, J. Wang, Z. Wen, W. Tang, Z. L. Wang, Standards and figure-of-merits for quantifying the performance of triboelectric nanogenerators. *Nat. Commun.* **6**, 8376 (2015).
20. Y. Long, Y. Yu, X. Yin, J. Li, X. Du, Y. Jiang, X. Wang, Effective anti-biofouling enabled by surface electric disturbance from water wave-driven nanogenerator. *Nano Energy* **57**, 558–565 (2019).
21. J. H. Ahn, J. Y. Hwang, C. G. Kim, G. H. Nam, K. K. Ahn, Unsteady streaming flow based TENG using hydrophobic film tube with different charge affinity. *Nano Energy* **67**, 104269 (2020).
22. R. K. Cheedarala, M. Shahriar, J. H. Ahn, J. Y. Hwang, K. K. Ahn, Harvesting liquid stream energy from unsteady peristaltic flow induced pulsatile flow-TENG (PF-TENG) using slipping polymeric surface inside elastomeric tubing. *Nano Energy* **65**, 104017 (2019).
23. D. Choi, S. Lee, S. M. Park, H. Cho, W. Hwang, D. S. Kim, Energy harvesting model of moving water inside a tubular system and its application of a stick-type compact triboelectric nanogenerator. *Nano Res.* **8**, 2481–2491 (2015).
24. Y. Liu, Y. Zheng, T. Li, D. Wang, F. Zhou, Water-solid triboelectrification with self-repairable surfaces for water-flow energy harvesting. *Nano Energy* **61**, 454–461 (2019).
25. L. Pan, J. Wang, P. Wang, R. Gao, Y.-C. Wang, X. Zhang, J.-J. Zou, Z. L. Wang, Liquid-FEP-based U-tube triboelectric nanogenerator for harvesting water-wave energy. *Nano Res.* **11**, 4062–4073 (2019).
26. X. Zhang, M. Yu, Z. Ma, H. Ouyang, Y. Zou, S. L. Zhang, H. Niu, X. Pan, M. Xu, Z. Li, Z. L. Wang, Self-powered distributed water level sensors based on liquid-solid triboelectric nanogenerators for ship draft detecting. *Adv. Funct. Mater.* **29**, 1900327 (2019).
27. W. Xu, H. Zheng, Y. Liu, X. Zhou, C. Zhang, Y. Song, X. Deng, M. Leung, Z. Yang, R. X. Xu, Z. L. Wang, X. C. Zeng, Z. Wang, A droplet-based electricity generator with high instantaneous power density. *Nature* **578**, 392–396 (2020).
28. H. Wu, Z. Wang, Y. Zi, Multi-mode water-tube-based triboelectric nanogenerator designed for low-frequency energy harvesting with ultrahigh volumetric charge density. *Adv. Energy Mater.* **11**, 2100038 (2021).
29. R. Lei, Y. Shi, Y. Ding, J. Nie, S. Li, F. Wang, H. Zhai, X. Chen, Z. L. Wang, Sustainable high-voltage source based on triboelectric nanogenerator with a charge accumulation strategy. *Energy Environ. Sci.* **13**, 2178–2190 (2020).
30. H. Wu, N. Mendel, S. van der Ham, L. Shui, G. Zhou, F. Mugele, Charge trapping-based electricity generator (CTEG): An ultrarobust and high efficiency nanogenerator for energy harvesting from water droplets. *Adv. Mater.* **32**, 2001699 (2020).
31. H. Wu, S. Wang, Z. Wang, Y. Zi, Achieving ultrahigh instantaneous power density of 10 MW/m^2 by leveraging the opposite-charge-enhanced transistor-like triboelectric nanogenerator (OCT-TENG). *Nat. Commun.* **12**, 5470 (2021).
32. N. Zhang, H. Gu, H. Zheng, S. Ye, L. Kang, C. Huang, K. Lu, W. Xu, Z. Wang, J. Zhang, X. Zhou, Boosting the output performance of volume effect electricity generator (VEEG) with water column. *Nano Energy* **73**, 104748 (2020).

33. S. Lin, M. Zheng, J. Luo, Z. L. Wang, Effects of surface functional groups on electron transfer at liquid-solid interfacial contact electrification. *ACS Nano* **14**, 10733–10741 (2020).
34. S. Xu, H. Guo, S. L. Zhang, L. Jin, W. Ding, X. Wang, Z. L. Wang, Theoretical investigation of air breakdown direct current triboelectric nanogenerator. *Appl. Phys. Lett.* **116**, 263901 (2020).
35. G. Cheng, H. Zheng, F. Yang, L. Zhao, M. Zheng, J. Yang, H. Qin, Z. Dua, Z. L. Wang, Managing and maximizing the output power of a triboelectric nanogenerator by controlled tip–electrode air-discharging and application for UV sensing. *Nano Energy* **44**, 208–216 (2018).
36. J. Luo, L. Xu, W. Tang, T. Jiang, F. Fan, Y. Pang, L. Chen, Y. Zhang, Z. L. Wang, Direct-current triboelectric nanogenerator realized by air breakdown induced ionized air channel. *Adv. Energy Mater.* **8**, 1800889 (2018).
37. D. Liu, X. Yin, H. Guo, L. Zhou, X. Li, C. Zhang, J. Wang, Z. L. Wang, A constant current triboelectric nanogenerator arising from electrostatic breakdown. *Sci. Adv.* **5**, eaav6437 (2019).
38. J. Wang, C. Wu, Y. Dai, Z. Zhao, A. Wang, T. Zhang, Z. L. Wang, Achieving ultrahigh triboelectric charge density for efficient energy harvesting. *Nat. Commun.* **8**, 88 (2017).
39. S. Wang, Y. Xie, S. Niu, L. Lin, C. Liu, Y. S. Zhou, Z. L. Wang, Maximum surface charge density for triboelectric nanogenerators achieved by ionized-air injection: Methodology and theoretical understanding. *Adv. Mater.* **26**, 6720–6728 (2014).
40. Y. Raizer, *Spark Discharge* (Routledge, 2017).
41. Z. L. Wang, A. C. Wang, On the origin of contact-electrification. *Mater. Today* **30**, 34–51 (2019).
42. F.-R. Fan, Z.-Q. Tian, Z. L. Wang, Flexible triboelectric generator. *Nano Energy* **1**, 328–334 (2012).
43. F. J. Hughes, Electrostatics: Principles, problems and applications. *Phys. Bull.* **38**, 424 (1987).
44. J. Nie, Z. Ren, L. Xu, S. Lin, F. Zhan, X. Chen, Z. L. Wang, Probing contact-electrification-induced electron and ion transfers at a liquid-solid interface. *Adv. Mater.* **32**, 1905696 (2020).
45. S. Lin, L. Xu, A. C. Wang, Z. L. Wang, Quantifying electron-transfer in liquid-solid contact electrification and the formation of electric double-layer. *Nat. Commun.* **11**, 399 (2020).
46. L. Zhang, X. Li, Y. Zhang, Y. Feng, F. Zhou, D. Wang, Regulation and influence factors of triboelectricity at the solid-liquid interface. *Nano Energy* **78**, 105370 (2020).
47. C. Xu, Y. Zi, A. C. Wang, H. Zou, Y. Dai, X. He, P. Wang, Y.-C. Wang, P. Feng, D. Li, Z. L. Wang, On the electron-transfer mechanism in the contact-electrification effect. *Adv. Mater.* **30**, 1706790 (2018).
48. J. P. Perdew, K. Burke, M. Ernzerhof, Generalized gradient approximation made simple. *Phys. Rev. Lett.* **77**, 3865–3868 (1996).
49. G. Kresse, J. Furthmüller, Efficient iterative schemes for *ab initio* total-energy calculations using a plane-wave basis set. *Phys. Rev. B* **54**, 11169–11186 (1996).
50. P. E. Blöchl, Projector augmented-wave method. *Phys. Rev. B* **50**, 17953–17979 (1994).
51. S. Grimme, J. Antony, S. Ehrlich, H. Krieg, A consistent and accurate *ab initio* parametrization of density functional dispersion correction (DFT-D) for the 94 elements H-Pu. *J. Chem. Phys.* **132**, 154104 (2010).
52. W. Tang, E. Sanville, G. Henkelman, A grid-based Bader analysis algorithm without lattice bias. *J. Phys. Condens. Matter* **21**, 084204 (2009).
53. E. Sanville, S. D. Kenny, R. Smith, G. Henkelman, Improved grid-based algorithm for Bader charge allocation. *J. Comput. Chem.* **28**, 899–908 (2007).
54. G. Henkelman, A. Arnaldsson, H. Jónsson, A fast and robust algorithm for Bader decomposition of charge density. *Comput. Mater. Sci.* **36**, 354–360 (2006).
55. M. Yu, D. R. Trinkle, Accurate and efficient algorithm for Bader charge integration. *J. Chem. Phys.* **134**, 064111 (2011).
56. M. Xu, P. Wang, Y.-C. Wang, S. L. Zhang, A. C. Wang, C. Zhang, Z. Wang, X. Pan, Z. L. Wang, A soft and robust spring based triboelectric nanogenerator for harvesting arbitrary directional vibration energy and self-powered vibration sensing. *Adv. Energy Mater.* **8**, 1702432 (2018).
57. X. Li, J. Tao, X. Wang, J. Zhu, C. Pan, Z. L. Wang, Networks of high performance triboelectric nanogenerators based on liquid-solid interface contact electrification for harvesting low-frequency blue energy. *Adv. Energy Mater.* **8**, 1800705 (2018).
58. P. Cheng, H. Guo, Z. Wen, C. Zhang, X. Yin, X. Li, D. Liu, W. Song, X. Sun, J. Wang, Z. L. Wang, Largely enhanced triboelectric nanogenerator for efficient harvesting of water wave energy by soft contacted structure. *Nano Energy* **57**, 432–439 (2019).
59. G. Liu, H. Guo, S. Xu, C. Hu, Z. L. Wang, Oblate spheroidal triboelectric nanogenerator for all-weather blue energy harvesting. *Adv. Energy Mater.* **9**, 1900801 (2019).
60. P. Rui, W. Zhang, Y. Zhong, X. Wei, Y. Guo, S. Shi, Y. Liao, J. Cheng, P. Wang, High-performance cylindrical pendulum shaped triboelectric nanogenerators driven by water wave energy for full-automatic and self-powered wireless hydrological monitoring system. *Nano Energy* **74**, 104937 (2020).
61. K. Xia, J. Fu, Z. Xu, Multiple-frequency high-output triboelectric nanogenerator based on a water balloon for all-weather water wave energy harvesting. *Adv. Energy Mater.* **10**, 2000426 (2020).
62. H. Wang, L. Xu, Y. Bai, Z. L. Wang, Pumping up the charge density of a triboelectric nanogenerator by charge-shuttling. *Nat. Commun.* **11**, 4203 (2020).
63. X. Liang, T. Jiang, G. Liu, Y. Feng, C. Zhang, Z. L. Wang, Spherical triboelectric nanogenerator integrated with power management module for harvesting multidirectional water wave energy. *Energy Environ. Sci.* **13**, 277–285 (2020).
64. X. Jiao, Z. Zhu, Y. Fan, H. Li, Z. L. Wang, Triboelectric charging at the nanostructured solid/liquid interface for area-scalable wave energy conversion and its use in corrosion protection. *ACS Nano* **9**, 7671–7677 (2015).
65. X. Zhang, Y. Zheng, D. Wang, F. Zhou, Solid-liquid triboelectrification in smart U-tube for multifunctional sensors. *Nano Energy* **40**, 95–106 (2017).
66. Q. Zhang, Q. Liang, Q. Liao, M. Ma, F. Gao, X. Zhao, Y. Song, L. Song, X. Xun, Y. Zhang, An amphiphobic hydraulic triboelectric nanogenerator for a self-cleaning and self-charging power system. *Adv. Funct. Mater.* **28**, 1803117 (2018).

Acknowledgments

Funding: This research was supported by the National Natural Science Foundation of China (nos. U21A2046, 51905518, and 52005292), the Program for Taishan Scholars of Shandong Province (no. ts20190965), the Western Light Project of CAS (xbzg-zdsys-202118), the Key Research Program of the Chinese Academy of Sciences (grant no. ZDBS-ZRKJZ-TLC010), and the Innovation Leading Talents Program of Qingdao (19-3-2-23-zhc) in China. Patents have been filed based on the research results presented here. **Author contributions:** D.W. conceived the idea. Y.D., C.Z., and S.X. analyzed the data and wrote the paper. D.W. and Z.L.W. supervised the research. L.Z. and N.L. fabricated the device. Y.F., N.W., and M.F. designed the materials of the device. Y.X., X.Z., and F.Z. helped with the experiments. All the authors discussed the results and commented on the manuscript. **Competing interests:** The authors declare that they have no competing interests. **Data and materials availability:** All data needed to evaluate the conclusions in the paper are present in the paper and/or the Supplementary Materials.

Submitted 18 May 2022
Accepted 12 October 2022
Published 30 November 2022
10.1126/sciadv.add0464

ScienceAdvances

Gas-liquid two-phase flow-based triboelectric nanogenerator with ultrahigh output power

Yang DongShiwei XuChi ZhangLiqiang ZhangDaoai WangYuanyuan XieNing LuoYange FengNannan WangMin FengXiaolong ZhangFeng ZhouZhong Lin Wang

Sci. Adv., 8 (48), eadd0464. • DOI: 10.1126/sciadv.add0464

Science Advances (ISSN) is published by the American Association for the Advancement of Science. 1200 New York Avenue NW, Washington, DC 20005. The title *Science Advances* is a registered trademark of AAAS.